A Bragg-Like Point Extraction Method for Co-polarization Channel Imbalance Calibration

Xingjie Zhao, Yunkai Deng, *Member, IEEE*, Hanglan Guo, Xiuqing Liu, Chunle Wang, and Guo Song

***Abstract*—Calibration by distributed targets is an important part of polarimetric calibration (PolCAL) without corner reflectors (CRs). Currently, both the correlation of HH and VV (R_{hhvv}) and the equivalent number of looks (ENL) constitute the common method for the extraction of Bragg-like points (BLPs) in order to calibrate the co-polarization channel imbalance k. However, strict assumptions about distributed targets and complex mathematical expressions regarding ENL limit the impact analysis of k on R_{hhvv} and ENL; thus, the fixed thresholds for R_{hhvv} and ENL can be obtained only by comparing the calibration errors with the CRs or simulated values in order to calibrate k accurately. In some Earth observation and lunar exploration without CRs, the abovementioned conditions are not satisfied. In this article, a BLP extraction method is proposed for calibrating co-polarization channel imbalance k in PolCAL. $H/\bar{\alpha}$ decomposition is utilized to deduce the specific scattering impacts of BLPs by different k values first. Then, a dynamic selection method is proposed to reduce the influence of fixed thresholds and improve the extraction accuracy. Multiscene polarimetric synthetic aperture radar images from AIRSAR, ALOS, and GF-3 are utilized to verify the effectiveness of the proposed algorithm in the extraction of BLPs and the calibration results of k obtained by applying the extracted BLPs.**

***Index Terms*—Bragg -like points (BLPs), co-polarization channel imbalance k, dynamic selection, $H/\bar{\alpha}$ decomposition, polarimetric synthetic aperture radar (PolSAR).**

NOMENCLATURE

Abbreviations

BLP	Bragg-like point.
CI	Channel imbalance.
CR	Corner reflector.
ENL	Equivalent number of looks.
Ext. BLP	Bragg-like point extracted from uncalibrated k polarimetric images.
POA	Polarization orientation angle.
PolCAL	Polarimetric calibration.
PolSAR	Polarimetric synthetic aperture radar.
UZH	Unitary zero helix.
XT	Crosstalk.

Variables

$\alpha_i/\beta_i/\sigma_i/\gamma_i/\xi_i$	Complex spherical coordinates.
$[C_3]$	Covariance matrix of $[S_3]$.
$C_{ij}(i,j=1,2,3)$	*i*th row and *j*th column element of $[C_3]$.
χ	Cross-polarization channel imbalance.
$\text{cod}_i(i=1,2)$	Ratio of the cross-polarization power to the co-polarization amplitude based on $[O]$.
$\text{cod}_j(j=3,4)$	Ratio of the cross-polarization power to the co-polarization amplitude based on $[C_3]$.
$\text{error}_{\text{amp}}$	Calculated amplitude error of k, whose unit is 1.
$\text{error}_{\text{amp\_dB}}$	Calculated amplitude error of k, whose unit is dB.
$\text{error}_{\text{pha}}$	Calculated phase error of k.
H	Polarimetric scattering entropy.
index_1	(Number of NZ9 points/number of points in a bin)*(number of BLPs in NZ9/number of NZ9 points)^2.
index_2	Number of BLPs in NZ9/number of NZ9 points.
$[K_{\text{amp3}}]$	$[K_3]$, where the phase of k is 0.
$[K_{\text{pha3}}]$	$[K_3]$, where the amplitude of k is 1.
$[K_3]$	Co-polarization channel imbalance matrix with reciprocity.
$[K_4]$	Co-polarization channel imbalance matrix without reciprocity.
k	Co-polarization channel imbalance value.
$\vec{k}_p$	Pauli basis.
$\vec{k}_i(i=1,2,3)$	Unit eigenvectors of $[T_3]$.
$\lambda_i(i=1,2,3)$	Eigenvalues of $[T_3]$.
$[M]$	Vector format of observation scattering matrix.
$[N_3]$	Normalized $[T_k]$.
$< N_{11} >$	First element of $[N_3]$.
$[O]$	Covariance matrix corresponding to $[M]$.
$[O_{\text{tri}}]$	Vector format of observation scattering matrix of a trihedral corner reflector.
$O_{ij}(i,j=1,2,3)$	*i*th row and *j*th column element of $[O]$.
$\varphi_{C_{13}}$	Phase of C_{13}.
φ_k	Phase of k.
$p_i(i=1,2,3)$	Pseudoprobability corresponding to H.
$[Q]$	Cross-polarization channel imbalance matrix.

Manuscript received 18 November 2022; accepted 28 February 2023. Date of publication 3 March 2023; date of current version 25 April 2023. This work was supported in part by the Beijing Municipal Natural Science Foundation under Grant 4192065 and in part by the National Natural Science Foundation of China under Grant 61901445. *(Corresponding author: Xiuqing Liu.)*

Xingjie Zhao, Hanglan Guo, and Guo Song are with the Department of Space Microwave Remote Sensing System, Aerospace Information Research Institute, Chinese Academy of Sciences, Beijing 100190, China, and also with the School of Electronic, Electrical and Communication Engineering, University of Chinese Academy of Sciences, Beijing 100049, China (e-mail: zhaoxingjie19@mails.ucas.ac.cn; guohanglan19@mails.ucas.ac.cn; songguo19@mails.ucas.ac.cn).

Yunkai Deng, Xiuqing Liu, and Chunle Wang are with the Department of Space Microwave Remote Sensing System, Aerospace Information Research Institute, Chinese Academy of Sciences, Beijing 100190, China (e-mail: ykdeng@mail.ie.ac.cn; lucia@mail.ie.ac.cn; clwang@mail.ie.ac.cn).

Digital Object Identifier 10.1109/JSTARS.2023.3252014

R_{hhvv}	Correlation of HH and VV.
R_{xc}	Threshold of $\text{cod}_i (i = 1, 2)$.
$[S_3]$	Vector format of the nondistorted scattering matrix with reciprocity.
$[S_{\text{tri}}]$	Vector format of the nondistorted scattering matrix of a trihedral corner reflector.
$[T_k]$	Coherency matrix corresponding to $[M]$.
T_{k11}	First element of $[T_k]$.
$u/v/w/z$	Crosstalk value.
$[X]$	Crosstalk matrix.
Y	Absolute radiometric gain.

I. Introduction

DUE to its backscatter sensitivity, polarimetric synthetic aperture radar (PolSAR) provides distinctive mapping ability for terrain categorization and ground-cover classification that are highly useful for the measurements and validations of snow, sea surface, forests, crops, and alternative environmental ground truth [1], [2], [3], [4]. To quantitatively analyze radar backscatter from the PolSAR system, it is important to determine the polarimetric distortion matrices (PDMs) of the PolSAR system, which is termed polarimetric calibration (PolCAL). PDMs can be separated into channel imbalance (CI) and crosstalk (XT) components when ignoring added instrument noise and Faraday rotation angle [5], [6], [7].

In practical PolCAL, corner reflectors (CRs) are considered the most accurate calibrators due to the fixed ratios among polarimetric channels [8], [9], [10], [11]. Considering different size requirements of the passive CRs in different bands and the high price of polarimetric active radar calibrators (PARCs), assumptions of distributed target scattering properties, such as reciprocity and reflection symmetry, are used in the calculations of the PDMs. However, in most PolCAL methods, appropriate natural distributed targets are used to determine the XT and cross-polarization (x-pol) CI, and the co-polarization (co-pol) CI k is determined by the use of one CR [7], [12], [13], [14], [15], [16], [17], [18], [19].

Due to the limitations of CRs, the calibration of k by distributed targets has become an interesting research field in recent years [20], [21], [22], [23], [24], [25], [26]. Significantly, Shi et al. [21], [24], [26] investigated the unitary zero helix (UZH) property of Bragg-like points (BLPs) for calibrating k that has been applied in many large-scale applications because BLPs, such as bare soil are widely distributed areas and present many stable characteristics in most PolSAR applications, such as Earth observation and lunar exploration. To the best of the our knowledge, the common and efficient method for extracting BLPs in uncalibrated k PolSAR data is to assign thresholds to the correlation of HH and VV (R_{hhvv}) and equivalent number of looks (ENL). However, as shown in Fig. 10 of [24], experiments indicate that the calibration error of k is greatly affected by different fixed thresholds, which may be close to 4 dB/12°. Therefore, the BLPs extraction may make the calibration accuracy of k unstable. In some PolCAL applications without CRs or other equipment, such as lunar exploration, ENL, and R_{hhvv} cannot directly be utilized to extract BLPs accurately. There are two main reasons for the unsatisfactory errors.

The first is that in the analysis of the effect of k on R_{hhvv} and the ENL, less general assumptions are applied so that these two parameters cannot be used directly in some polarimetric applications. For the distortion-immune property of R_{hhvv}, two conditions must be satisfied: 1) The second-order term of XT can be ignored if the XT of a PolSAR system is lower than -20 dB; 2) The cross-correlation coefficient is small enough, which means that the selected area should satisfy the reflection symmetry assumption as much as possible. However, this hypothesis is strong in high-resolution PolSAR, which may impact the polarization orientation angle (POA) accuracy if R_{hhvv} is utilized to extract the BLPs [24]. For the application of the ENL to practical PolCAL, the ENL is considered to be less sensitive to system distortion [24]. In some PolSAR applications, such as lunar exploration by PolSAR systems that require accurate calibration of k without CRs, it is necessary to analyze the impact of k on the ENL as a basis for extracting BLPs. However, the expression for the ENL is quite complicated and involves second-order statistics varying with k [26]. Therefore, it is difficult to analyze the effect of k on ENL. The other reason is that only fixed thresholds on R_{hhvv} and the ENL are set. Since the influence of k on R_{hhvv} and the ENL is unclear, selection of the fixed thresholds can be based only on the comparison with simulated values or CR results, producing the threshold corresponding to the minimum values. However, the optimal thresholds may vary among PolSAR images, so that the application of the same thresholds in all PolCAL without CRs may cause BLPs selection errors and k calibration errors.

The first contribution of this article is that polarimetric scattering entropy H and polarimetric scattering $\bar{\alpha}$ parameter are utilized to replace R_{hhvv} and the ENL for BLPs extraction from uncalibrated k PolSAR images. In $H/\bar{\alpha}$ decomposition [27], H and $\bar{\alpha}$ divide the ground targets into eight parts, where Zone 9 (Z9, $H \leq 0.5$ and $\bar{\alpha} \leq 42.5°$) is the Bragg-like scattering area with low helix scattering power. In addition, the two parameters are roll invariant, making the strict reflection symmetry assumption in the extraction of BLPs unnecessary for ground targets. Furthermore, H and $\bar{\alpha}$ have clear mathematical expressions and two-dimensional representations ($H/\bar{\alpha}$ plane), enabling convenient analysis of the impact of k.

The second contribution of this article is the dynamic extraction of BLPs from uncalibrated k PolSAR data. Since the fixed thresholds directly determine the extracted BLPs (ext. BLPs), affecting k calibration accuracy, we propose that after initially extracting most of the BLPs through thresholds, k values with different amplitudes and phases are added to the uncalibrated k PolSAR image to make the points move on the $H/\bar{\alpha}$ plane so that some BLPs that are previously not extracted by thresholds are selected in the proposed method and that the points with wrong features selected by thresholds are eliminated. Ultimately, the selected areas are highly consistent with the BLPs. We note that we do not object to selecting the BLPs by setting thresholds for the polarimetric parameters, but an additional process is required to improve the accuracy of the ext. BLPs after the use of the thresholds for preliminary selection.

The rest of this article is organized as follows. Section II introduces the effect of k on H and $\bar{\alpha}$; Section III proposes a method for choosing the BLPs; Section IV presents the experimental results; and Section V provides discussion. Finally, Section VI concludes this article.

II. Effect of k on H and $\bar{\alpha}$

This section mainly introduces the effect of k on H and $\bar{\alpha}$. First, the calibration model and the concepts of H and $\bar{\alpha}$ are briefly introduced, and then the variation range of k is limited by the preliminary calibration results of the well-known PolSAR systems. Through the properties of the Hermitian matrix and the relationship between the normalized coherence matrix $[N_3]$[28] and $\bar{\alpha}$, the relationship of the phase of k (φ_k) to H and $\bar{\alpha}$ is derived. Finally, Monte Carlo simulations are utilized to obtain the change in the Z9 lateral area on the $H/\bar{\alpha}$ plane caused by the amplitude of k.

A. PolCAL Model

During the normal operation of the PolSAR system, the receiving and transmitting channels interact with each other due to the effects of the external environment and various system factors, such as XT, CI, Faraday rotation, and system noise, resulting in an observation scattering matrix $[M]$. Considering that the Faraday rotation matrix can be solved by the measurement of the total electron content and calm water can be used to estimate the noise matrix [22], [29], the rest of PDMs superimposed on the nondistorted scattering matrix $[S_3]$ can be expressed by [21]

$$\begin{aligned}[M] &= Y\,[X]\,[Q]\,[A_4]\,[K_3]\,[S_3] \\ &= Y \begin{bmatrix} 1 & w & v & wv \\ u & 1 & uv & v \\ z & wz & 1 & w \\ uz & z & u & 1 \end{bmatrix} \begin{bmatrix} \chi & 0 & 0 & 0 \\ 0 & \chi & 0 & 0 \\ 0 & 0 & 1 & 0 \\ 0 & 0 & 0 & 1 \end{bmatrix} \\ &\quad \times \begin{bmatrix} 1 & 0 & 0 \\ 0 & 1/\sqrt{2} & 0 \\ 0 & 1/\sqrt{2} & 0 \\ 0 & 0 & 1 \end{bmatrix} \begin{bmatrix} k^2 & 0 & 0 \\ 0 & k & 0 \\ 0 & 0 & 1 \end{bmatrix} \begin{bmatrix} S_{\mathrm{HH}} \\ \sqrt{2}S_{\mathrm{HV}} \\ S_{\mathrm{VV}} \end{bmatrix} \end{aligned} \tag{1}$$

where, u, v, w, and z are related to the XT; χ is the x-pol CI; and Y denotes the absolute radiometric gain. Notably, Y is common to all channels and is not considered to be a part of PolCAL in this article. Therefore, the covariance matrix corresponding to $[M]$ becomes

$$\begin{aligned}[O] &= [M]\,[M]^{\dagger} \\ &= [X]\,[Q]\,[A_4]\,[K_3]\,[C_3]\,([X]\,[Q]\,[A_4]\,[K_3])^{\dagger} \end{aligned} \tag{2}$$

where, $[C_3]$ is the covariance matrix corresponding to $[S_3]$ and $\dagger$ represents the vector conjugate transpose operator.

B. $H/\bar{\alpha}$ Decomposition

As a type category of eigenvalue-based decomposition [27], [30], [31], $H/\bar{\alpha}$ decomposition can be described by explicit and physically meaningful mathematical expressions, providing a possibility to extract BLPs in Z9 from uncalibrated k PolSAR images.

For processing PolSAR signals, the coherency matrix $[T_3]$ is obtained as a matrix producing the conjugate transpose of the Pauli basis $\vec{k_p}$ with itself. In the actual situation, since the targets are coherent on PolSAR images, it is necessary to perform a multilook operation for $[T_3]$. The corresponding mathematical model can be written as

$$[T_3] = \langle \vec{k_p} \cdot \vec{k_p}^{\dagger} \rangle \tag{3}$$

$$\vec{k_p} = \frac{1}{\sqrt{2}} \begin{bmatrix} S_{\mathrm{HH}} + S_{\mathrm{VV}} & S_{\mathrm{HH}} - S_{\mathrm{VV}} & 2S_{\mathrm{HV}} \end{bmatrix}^T \tag{4}$$

where, $\langle \cdot \rangle$ represents multilook processing and the superscript T is the vector transpose operator. As [27] mentioned previously, (3) can be written combining the eigenvalue λ_i and the unit eigenvector $\vec{k_i}$ as

$$[T_3] = \lambda_1 \vec{k_1} \vec{k_1}^{\dagger} + \lambda_2 \vec{k_2} \vec{k_2}^{\dagger} + \lambda_3 \vec{k_3} \vec{k_3}^{\dagger}. \tag{5}$$

In the complex spherical coordinate system defined by α_i, β_i, σ_i, γ_i, and ξ_i, $\vec{k_i}(i = 1, 2, 3)$ can be written as

$$\vec{k_i} = e^{j\xi_i} \begin{bmatrix} \cos\alpha_i & \sin\alpha_i \cos\beta_i e^{j\sigma_i} & \sin\alpha_i \sin\beta_i e^{j\gamma_i} \end{bmatrix}^T \tag{6}$$

where, j denotes $\sqrt{-1}$. The pseudoprobability is defined as

$$p_i = \lambda_i \Big/ \sum_{i=1}^{3} \lambda_i. \tag{7}$$

Furthermore, the polarimetric scattering $\bar{\alpha}$ parameter and polarimetric scattering entropy H can be expressed as

$$\bar{\alpha} = \sum_{i=1}^{3} p_i \alpha_i \tag{8}$$

$$H = -\sum_{i=1}^{3} p_i \log_3 p_i. \tag{9}$$

In the $H/\bar{\alpha}$ plane [30], Z9 represents the low-entropy surface area and mainly includes geometric optic and physical optic surface scattering, namely Bragg surface scattering and specular scattering. The surfaces of natural targets, such as ice surfaces, water bodies, and very smooth land surfaces, are included. Considering that one task of PolCAL is long-term system monitoring, stable natural features in most image scenes should be utilized to calibrate PolSAR systems to avoid additional errors caused by excessive changes. Because of the variable natural climate and different penetrability of wavebands, the water body has more physical forms and complex changes than other Bragg surface scatters and thus is more suitable to remove the ice and water of Z9 for calibration.

C. Phase Effect of k on the $H/\bar{\alpha}$ Plane

Because of the existence of k, the polarimetric scattering characteristics reflected on the $H/\bar{\alpha}$ plane are inconsistent with the nondistorted targets. Next, we focus on the examination of point changes, with Z9 as the centre, in Z7, Z8, and Z9 (vertical

axis direction) and Z6 and Z9 (horizontal axis direction) [30] after adding the different values of k. Note that setting the range of k is vital because it directly determines the applicability of the proposed algorithm. In some well-known PolSAR systems, such as SIR-C [32], ALOS [33], RADARSAT-2 [34], and GF-3 [35], k or the corresponding received CI obtained during the preliminary calibration results have amplitude -2 to 2 dB and phase -180° to 180°. Therefore, in the following we use a -2 to 2 dB amplitude and -180° to 180° phase of k to illustrate the scattering characteristic variations of the targets on the Z9 of the $H/\bar{\alpha}$ plane.

First, the influence on the $H/\bar{\alpha}$ plane is explained by φ_k. Since the PolCAL process usually determines u, v, w, z, and χ and then determines k, it can be assumed that $u = v = w = z = 0$ and $\chi = 1$ when studying only the impact of k. Of note, calibrating u, v, w, z, and χ produces residual errors prior to calibrating k, slightly affecting the selection and use of BLPs for calibration. Analysis of this effect is described in detail in Section V. Considering that $[A_4]$ does not affect the relationship between the different channels, (2) can be expressed as

$$[O] = [K_3]\,[C_3]\,[K_3]^\dagger = \begin{bmatrix} k^2 & 0 & 0 \\ 0 & k & 0 \\ 0 & 0 & 1 \end{bmatrix} [C_3] \begin{bmatrix} k^2 & 0 & 0 \\ 0 & k & 0 \\ 0 & 0 & 1 \end{bmatrix}^\dagger . \tag{10}$$

When the amplitude of k is constant, (10) suggests that φ_k does not affect the real eigenvalues of $[O]$. The detailed derivation is given in the Appendix. Since the eigenvalues of the covariance matrix and corresponding coherency matrix are the same and H consists only of the eigenvalues of the coherency matrix, H is not affected by φ_k.

After considering the influence on H by φ_k, in the following we use the normalized coherency matrix $[N_3]$ to derive the $\bar{\alpha}$ change in targets when the amplitude of k is constant and the phase changes. $\langle N_{11} \rangle$, which is the first element of $[N_3]$, can be obtained by

$$\langle N_{11} \rangle = \frac{T_{k11}}{Tr\,\langle O \rangle} = \frac{C_{11}\,|k|^4 + C_{31}\,(k^*)^2 + C_{13}k^2 + C_{33}}{2\left(|k|^4\,C_{11} + |k|^2\,C_{22} + C_{33}\right)} \tag{11}$$

where, T_{k11} is the first element of the coherence matrix $[T_k]$ corresponding to $[O]$, $Tr\,\langle\cdot\rangle$ represents the trace of a matrix, and $C_{ij}(i, j = 1, 2, 3)$ represents the element in the ith row and jth column of $[C_3]$. When the amplitude of k remains unchanged and the phase changes, the varying term in (11) can be described by

$$\frac{1}{2}\left(C_{31}\,(k^*)^2 + C_{13}k^2\right) = |C_{13}|\,|k|^2 \cos\left(\varphi_{C_{13}} + 2\varphi_k\right). \tag{12}$$

The abovementioned equation indicates that $\langle N_{11} \rangle$ is the periodic variation of the trigonometric function with the change in φ_k and that there is at least one monotonic increasing process and one monotonic decreasing process in a period, whose value is 180°. To the best of our knowledge, obtaining the specific relationship between $\langle N_{11} \rangle$ and $\bar{\alpha}$ is challenging. However, the boundary can be described by three kinds of extreme conditions [36], allowing us to better understand that there is a decreasing relationship between $\langle N_{11} \rangle$ and $\bar{\alpha}$ in the statistical sense. Therefore, $\bar{\alpha}$ also exhibits a periodic trigonometric change, and the period is 180°.

D. Amplitude Effect of k on the $H/\bar{\alpha}$ Plane

Since the phase of k deduced in the previous section changes only in the longitudinal area of Z9 (Z7, Z8, and Z9), the change in the lateral area points of Z9 (Z6 and Z9) caused by the amplitude of k is analyzed in the following Monte Carlo experiments. The whole process can be divided into five steps that include first finding the boundary of Z6 ($0.51 < H < 0.52$ and $38^\circ < \bar{\alpha} < 40^\circ$) as the seed points, then simulating the surrounding PolSAR data of the seed points [37], [38], [39], adding an amplitude of -2 to 2 dB of k for the simulated Z6 points in the third step, observing the depth of the Z6 points to Z9 in the abscissa direction in the fourth step, and finally obtaining the influence of the Z6 points on Z9.

In Fig. 1, the experimental results after the addition of different k values are provided to simulate the impact performance on Z9 by Z6 points. Fig. 1(e) represents the nondistorted H and $\bar{\alpha}$ characteristics of the simulation points. In addition to the generated Z6 points (rose red), some of the Z9 (blue) and Z5 (yellow) and very few Z2 points (green) are also derived from the seed points. It is observed that 1) the rules obtained by each group of points are not the same, and there is rarely a uniform rule that covers them; 2) although k affects the distance from the point on the Z6 area to the $\bar{\alpha}$-axis, the shortest value is 0.33593. The boundary of Z6 and Z9 can be set at 0.33593 in the uncalibrated k images so that all points in the range of 0 to 0.33593 of H are not affected by the Z6 points. In the $H/\bar{\alpha}$ plane, the area with $H < 0.33593$ and $\bar{\alpha} < 42.5^\circ$ is defined as NZ9.

Through the abovementioned analysis, on the $H/\bar{\alpha}$ plane, with the Z9 area as the centre, the longitudinal change mainly depends on φ_k, and the horizontal change mainly depends on the amplitude of k. In particular, as the amplitude of k varies from -2 to 2 dB, the points on Z6 have a minimum entropy of 0.33593 so that there are no points of Z9 and points of Z6 mixed together in the entropy interval of 0 to 0.33593. After clearly recognizing the law, we can use the abovementioned proof to extract the BLPs exactly.

III. Methodology

The previous section describes the theoretical basis for selecting BLPs, focusing on the impact of k on the $H/\bar{\alpha}$ plane, particularly the horizontal and vertical regions that are the center of Z9. Based on these theories and derivations, the following focuses on a new dynamic BLPs extraction algorithm in the uncalibrated k PolSAR images to compensate for the selection and calibration error caused by only using thresholds of ENL and R_{hhvv}. A detailed flowchart is displayed in Fig. 2.

A. Influence of Z9 Horizontal Area Point Elimination

Due to the amplitude influence of k on H, the scattering points in Z6 are moved to Z9, affecting the selection of BLPs. However, when the amplitude of k varies from –2 to 2 dB, there is a minimum H of the original points in Z6, which is 0.33593. Considering φ_k does not affect H change of points on the $H/\bar{\alpha}$,

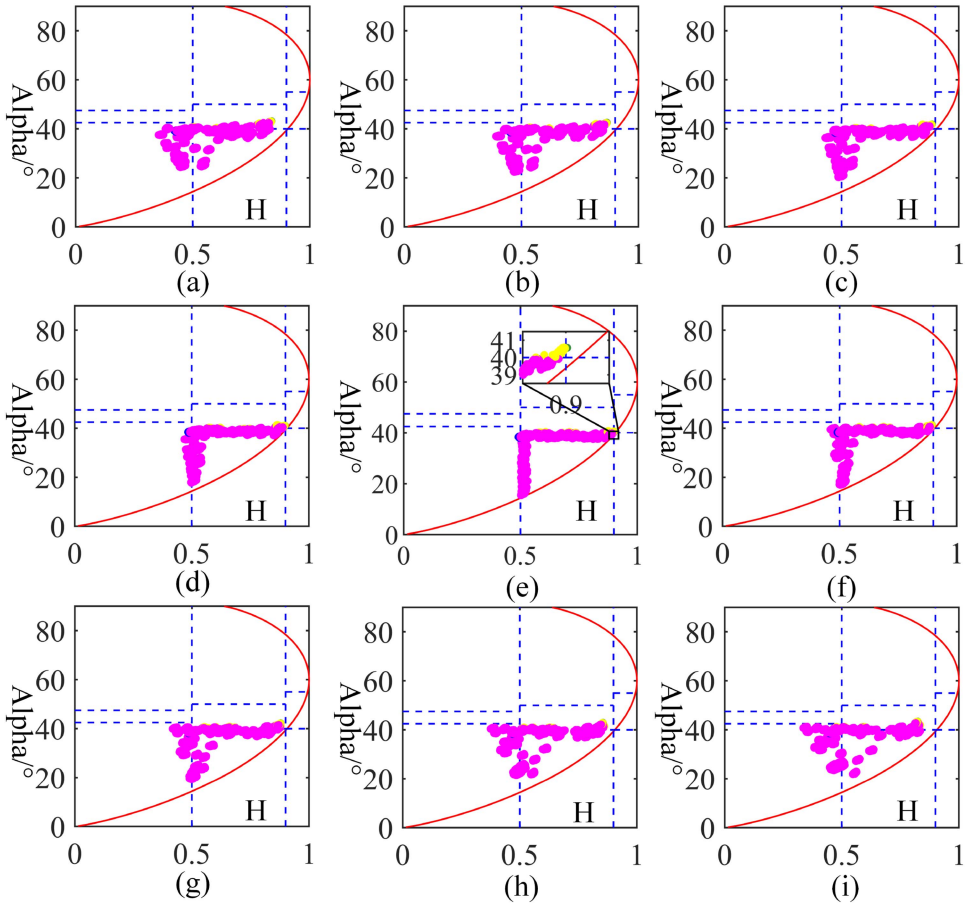

Fig. 1. Results after the addition of k to the simulated data. (a)–(i) Amplitudes of the 0.5 dB linear increase from -2 to 2 dB and 0° φ_k.

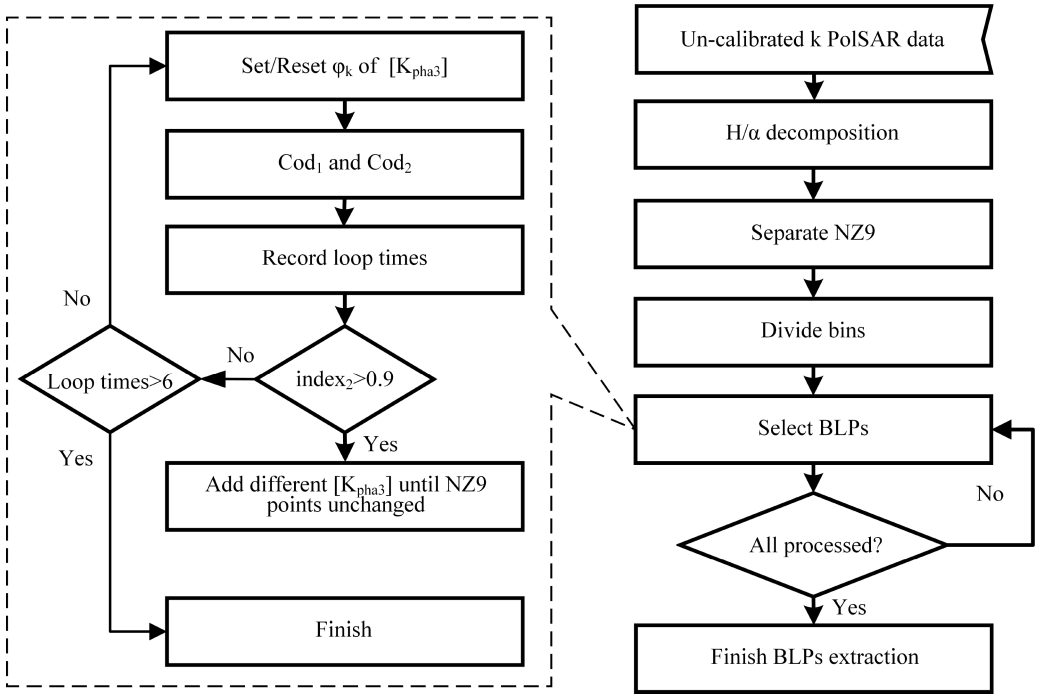

Fig. 2. Flowchart of selecting BLPs by the proposed method.

direct extraction of BLPs in the previously defined NZ9 can eliminate the errors of the selection of BLPs and calibration of k. Therefore, we extract the BLPs in NZ9 to eliminate the influence of the Z6 points. Note that there may be BLPs in other parts of Z9 except NZ9 (for example $0.33593 < H < 0.5$ and $\bar{\alpha} < 42.5°$), resulting in a smaller number of BLPs selected than the one in the entire PolSAR image. However, in PolCAL, the focus of extracting BLPs is primarily on the correct rate rather than the number of selected points. The related experimental results are shown in Section IV.

B. Influence of Z9 Longitudinal Area Point Elimination

In the following process, we divide uncalibrated k PolSAR images into different bins along the range and azimuth directions after taking into account the lack of drift along the azimuth direction and the presence of drift along the range direction of the PolSAR system [24]. According to (12), when the amplitude of k is constant and the phase changes uniformly from $-180°$ to $180°$, the points on the $H/\bar{\alpha}$ plane exhibit an oscillatory cosine movement with a period of $180°$. Since the cosine function does not vary monotonically from $-180°$ to $180°$, we cannot determine how the points change on the $H/\bar{\alpha}$ plane specifically when φ_k increases. Therefore, the following describes the preliminary selection of BLPs using the threshold, and more BLPs are extracted by using the change trend of the number of BLPs caused by the phase of k. The specific steps for the division into azimuth bins in a range cell are as follows.

Step 1: First, add $[K_{\text{pha3}}]$ with an amplitude of 0 dB and different phases φ_k to $[O]$ for the up-and-down movements of points on the $H/\bar{\alpha}$ plane that can be expressed as

$$[O_{\text{add}}] = [K_{\text{pha3}}]\,[O]\,[K_{\text{pha3}}]^{\dagger} \tag{13}$$

where, φ_k in $[K_{\text{pha3}}]$ is $\pm 45°$.

Step 2: Then, in NZ9, use the polarimetric parameters to set thresholds to find the approximate BLPs, given by [21]

$$\begin{aligned} \text{cod}_1 &= 10 * \log_{10}\left(\frac{|O_{22}|^2}{|O_{11}|}\right) \\ \text{cod}_2 &= 10 * \log_{10}\left(\frac{|O_{22}|^2}{|O_{33}|}\right) \end{aligned} \tag{14}$$

and set the same threshold R_{xc}, i.e.,

$$\begin{cases} \text{cod}_1 \le R_{\text{xc}} \\ \text{cod}_2 \le R_{\text{xc}} \end{cases} \tag{15}$$

the meaning of "Approximate" is that the threshold cannot completely select the BLPs in NZ9 and that there may be points in some other areas, such as Z7 and Z8 of the $H/\bar{\alpha}$ plane, that are selected by the thresholds set.

Step 3: As mentioned previously, in the process of extracting BLPs in NZ9, the proportion of BLPs to the NZ9 points and the number of NZ9 points are two key factors, with the former more important than the latter. Therefore, we set the parameter index_1:**(number of NZ9 points/number of points in a bin)*(number of BLPs in NZ9/number of NZ9 points)**^{2} based on several bins in a range cell to select the bin corresponding to the maximum value. At the same time, to prevent the second item of index_1 from being too small, index_2: **number of BLPs in NZ9/number of NZ9 points** must be greater than 0.9.

Step 4: If index_2 is less than 0.9, which reflects excessive or insufficient angle displacement in the actual situation, there is no significant aggregation of BLPs in NZ9. Therefore, the initial values must be reset. Based on $\pm 45°$, $\pm 45°/2^1$ is added to each value and the operations in Steps 1 to 3 are repeated. If index_2 is still not satisfied by the current calculated angles, $\pm 45°/2^2$ is added to each of the previous values. In addition, a termination condition is set when the number of loops is 6, which means the adding angle is less than $1°$ so that the points in NZ9 no longer change. However, this condition is inconsistent with the goal of this article, which is to select the most accurate points. Therefore, this range cell does not participate in PolCAL to reduce the error of k calculated.

Step 5: Through the processing of Steps 1 to 4, most of the BLPs eventually move to NZ9. Since adjusting φ_k implies moving the points on the $H/\bar{\alpha}$ plane up and down as a whole, if most of the BLPs move to NZ9, the scattering feature points representing Z7 and Z8 in nondistorted PolSAR images are also moved to their corresponding area. Therefore, the next step is to repeat Steps 1 to 4 and then observe whether the number of NZ9 points is the same as the number of points calculated previously. If so, this suggests that the maximum number of BLPs have been found in this range direction; if the number is larger or smaller, we repeat Steps 1 to 4 until the maximum point number of NZ9 is found.

During the dynamic extraction process, φ_k provides the driving force for movement, R_{xc} provides the movement trend of BLPs, index_1 provides the suitable bin position, and index_2 provides an extra guarantee for index_1. R_{xc} and index_2 are the intermediate parameters of the dynamic extraction process that have no direct impact on the number of final extraction points, as will be analyzed in Section V.

IV. Experiments and Results

In this section, calibrated full-PolSAR images are used to prove the practicability of the proposed algorithm, which are C-band GF-3 Quad-Polarization Strip I (QPSI) data, L-band ALOS full-PolSAR data, and L-band AIRSAR full-PolSAR data with corresponding C-band DEM data. Fig. 3 shows the location details of the experimental data. Whether CRs exist is used to divide these PolSAR images into different parts of these experiments. The PolSAR image with CRs is marked with red stars in Fig. 3(a).

For the PolSAR data without CRs, we add different amplitudes and phases of k to the images as the simulated datasets to derive BLPs in uncalibrated k PolSAR images. Then, BLPs are extracted by the proposed method and ENL and R_{hhvv} and the position of the ext. BLPs in $H/\bar{\alpha}$ plane is utilized to determine the correctness of the extraction algorithms. Finally, since the BLPs extraction algorithm proposed in this article aims to reduce the error of the potential calibration k caused by the inaccurate selection, these two ext. BLPs are utilized to calibrate

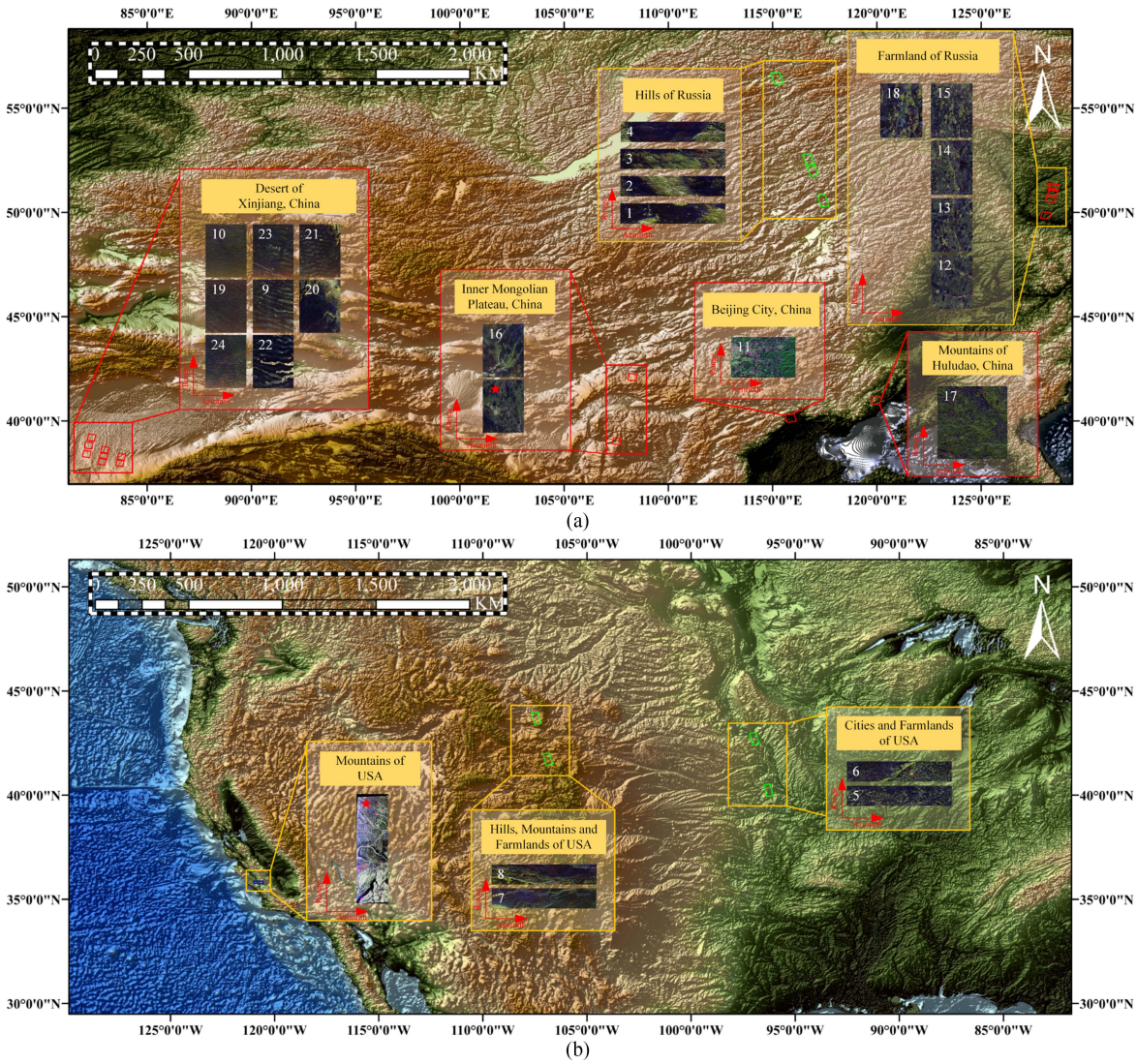

Fig. 3. Geographic extent of the 26 PolSAR images on a topographic map. The red, green, and blue boxes represent GF-3, ALOS, and AIRSAR data, respectively. The thumbnail of these PolSAR data and the brief introduction to the terrain are also shown in the figure. The white numbers from 1 to 24 and red stars are the marks of the PolSAR data.

k by using UZH [24] to confirm the validity of the extraction method.

For PolSAR images with CRs, the Ainsworth (Ans), Zero-Ans, and Quegan algorithms [12], [13] are utilized to evaluate and correct u, v, w, z, and χ first. Second, the ext. BLPs from the proposed method and ENL and R_{hhvv} are utilized to evaluate k by using UZH [24]. Then, we can obtain $[O]$ of trihedral CRs to compare with the CRs from the calibration models from the PolSAR images. Finally, the calculated XT and CI are added to the relative backscatter of the ideal trihedral CRs and compared with the relative backscatter of the trihedral CRs in the PolSAR data to verify the calibration k errors by the ext. BLPs. According to the description and derivation in the appendix of [26], if the noise matrix $[N]$ is not added to the calibration model in (1), the expression can still be written in the form of (1) for the PolSAR image after calibrating XT and CI.

In this article, R_{upper} and B_{lower}, which are the thresholds of R_{hhvv} and the ENL, are set to 0.8 and 0.7 [24], respectively, and R_{xc} is set to -20 dB. In the following section, we call the proposed method Halpha-UZH and the ENL and R_{hhvv} Shi-UZH, respectively.

A. Simulated Datasets

In this part, different values of k are added into the PolSAR images along the range direction. According to the number of range bins, we linearly add k with an amplitude of -2 to 2 dB and a phase of $-180°$ to $180°$. First, the AIRSAR data are analyzed using the algorithm of this article to introduce the process of the Halpha-UZH in detail; the data are marked by the red stars in Fig. 3(b).

Since there is some prominent noise in the far range and some black areas without data in the AIRSAR image, these parts have been cropped in this experiment and the final size of the data along the azimuth and range directions is 1200×800. A 7×7 multilook operation is performed on the data to obtain the

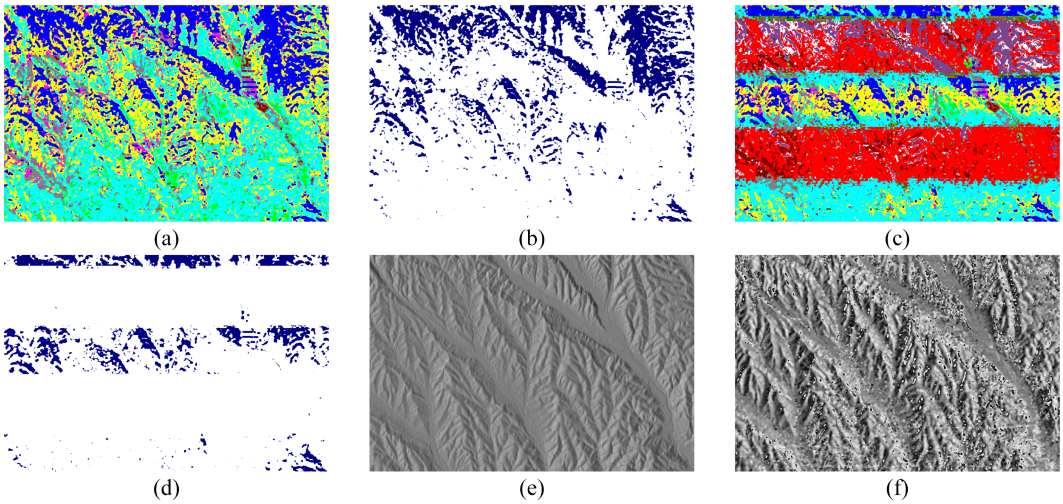

Fig. 4. Results for AIRSAR data. (a) $H/\bar{\alpha}$ decomposition image of real AIRSAR data. (b) BLPs derived from the $H/\bar{\alpha}$ decomposition image. (c) $H/\bar{\alpha}$ decomposition image for simulated uncalibrated k PolSAR data. (d) BLPs derived from the $H/\bar{\alpha}$ decomposition image using simulated uncalibrated k PolSAR data. (e) DEMPOA image. (f) POA image derived from the PolSAR image according to the true k.

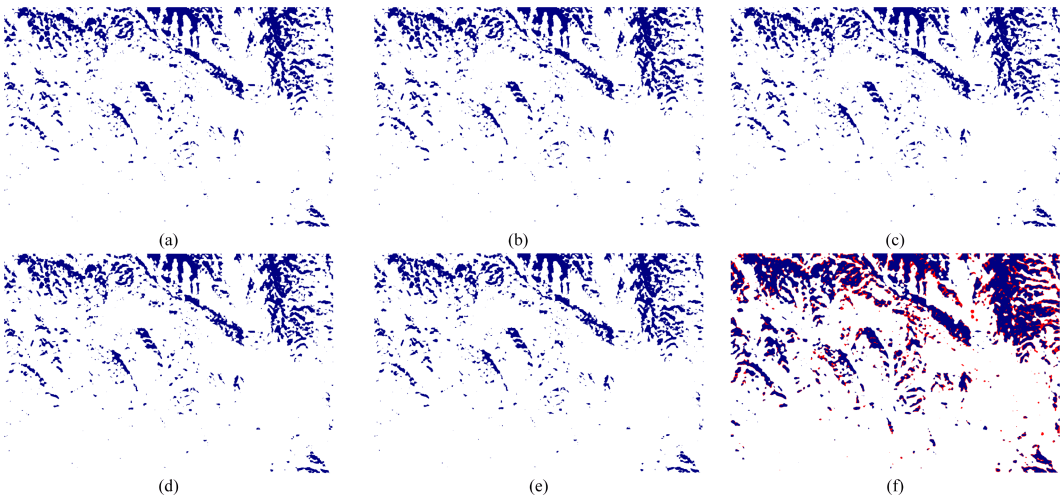

Fig. 5. Results of the BLPs selected under different azimuth bins: (a–e) show the results for 12, 15, 20, 30, and 60 bins, (f) represents the ext. BLPs from Shi-UZH, where the blue and red dots, respectively, indicate correct and incorrect points.

covariance matrix. The $H/\bar{\alpha}$ decomposition of the AIRSAR image is presented in Fig. 4(a), where the dark blue area represents BLPs on the $H/\bar{\alpha}$ plane, as shown in Fig. 4(b). Fig. 4(c) shows the $H/\bar{\alpha}$ decomposition of the PolSAR image with the addition of different k. After adding different k to the data along the range direction, the backscatter characteristics of the ground targets are quite inaccurate. The results for the $H/\bar{\alpha}$ decomposition directly solved for the Z9 to extract BLPs is shown in Fig. 10(d). The comparison of Fig. 10(d) and (b) indicates that it is difficult to directly obtain the BLPs from the uncalibrated k PolSAR data.

Fig. 5 shows the results of the BLPs selected under different azimuth bins by the algorithm mentioned in this article. Fig. 5(a)–(e) shows that the numbers of azimuth bins are 12, 15, 20, 30, and 60, respectively. Interestingly, the number of ext. BLPs, the number of real BLPs, and the percentage of real BLPs in ext. BLPs (Table I, rows 2–5, columns 2–6) are the same when dividing the AIRSAR image into different bins along the azimuth direction. This is because after the initial filtering of BLPs by the thresholds of cod_1, cod_2, and index_2 in NZ9, various φ_k are added to the points on the $H/\bar{\alpha}$ plane to move up and down in Step 5 until the number of points in NZ9 remains unchanged. Notably, it is important that the number of ext. BLPs is constant when dividing into different bins along the azimuth direction, so as not to introduce additional errors to UZH for calibrating k.

Fig. 5(f) shows the ext. BLPs obtained by Shi-UZH, where blue and red points, respectively, indicate the correct and incorrect points according to the $H/\bar{\alpha}$ decomposition of the original calibrated PolSAR image. The number of ext. BLPs and the number of real BLPs in ext. BLPs (Table I, column 7, rows 2–3) are greater than the corresponding values for Halpha-UZH. However, the percentage of real BLPs in ext. BLPs is lower and is approximately 16%. Therefore, the accuracy of Halpha-UZH is higher than that of Shi-UZH when calibrating the preliminary

TABLE I
BLP SELECTION RESULTS OF DIFFERENT AZIMUTHS AND RANGES BY THE PROPOSED ALGORITHM. THE FIRST ROW REPRESENTS THE BIN NUMBERS IN THE AZIMUTH DIRECTION. THE SECOND ROW REPRESENTS THE NUMBER OF EXT. BLPS. THE THIRD ROW REPRESENTS THE NUMBER OF REAL BLPS IN THE EXT. BLPS. THE FOURTH ROW REPRESENTS THE PERCENTAGE OF REAL BLPS IN EXT. BLPS. THE FIFTH ROW REPRESENTS THE COMPUTATIONAL COST REPRESENTED BY THE PROGRAM RUNNING TIME

	12	15	20	30	60	Shi-UZH
Ext. BLPs	113901	113901	113901	113901	113901	209297
Real BLPs in the ext. BLPs	113815	113815	113815	113815	113815	173522
Real BLPs in the ext. BLPs (%)	99.92450	99.92450	99.92450	99.92450	99.92450	82.90707
Computational cost (s)	9.14	8.45	9.01	8.73	9.06	1.54

TABLE II
SHI-UZH ERROR VERSUS HALPHA-UZH ERROR IN THE AMPLITUDE AND PHASE OF THE SIMULATED k. THE CORRESPONDING AMPLITUDE (DB) AND PHASE (°) ERROR ARE LISTED FOR DIFFERENT AZIMUTH AND RANGE BINS. THE CASES WHERE SHI-UZH IS BETTER THAN HALPHA-UZH ARE MARKED IN BOLD. THE LAST TWO ROWS REPRESENT THE MEAN AND STANDARD DEVIATION OF ROWS 4–8

		Shi-UZH		Halpha-UZH		Shi-UZH		Halpha-UZH	
		Amplitude	Phase	Amplitude	Phase	Amplitude	Phase	Amplitude	Phase
Range bins		80				100			
Azimuth bins	12	0.581	5.4222	0.4846	2.6492	0.7983	5.4195	0.7901	5.1527
	15	1.0797	4.7927	1.0559	4.3948	1.9591	8.3293	1.0196	4.5018
	20	0.8261	**2.5049**	0.4639	**3.0016**	**0.8563**	9.9133	**1.3776**	4.8011
	30	0.9461	*24.2814*	0.3255	0.8671	0.8168	*21.9747*	0.4113	3.1576
	60	0.8299	*11.3952*	0.1011	5.157	2.0450	4.7737	0.5999	2.4701
Mean		0.8526	9.6793	0.4862	3.2139	1.2951	10.0821	0.8397	4.0167
Std		0.1645	7.8694	0.3160	1.4860	0.5782	6.2362	0.3362	1.0268

results of k by UZH. It should be noted that when UZH is used for calibration, first-order fitting will be performed on the preliminary results to eliminate the influence of the selected Bragg-like point error as much as possible in order to acquire the final solution. However, fitting will only work on data with small deviations. If the accuracy of the selected area is not high, resulting in a large deviation between the k results of the preliminary solution and the real values, the fitting will not reduce the error, and may even increase the error. Therefore, if the ext. BLPs by Halpha-UZH are brought into UZH conditions for calibration, the accuracy of the final solution is higher than that for Shi-UZH.

The last row in Table I shows the program running times for Halpha-UZH and Shi-UZH. Clearly, Halpha-UZH is slower than Shi-UZH. However, the average selection time for BLPs by Halpha-UZH is less than 10 s, which is acceptable in practical applications, particularly when the accuracy of BLPs selection is the primary consideration.

Following the selection of BLPs by Shi-UZH and Halpha-UZH, since the numbers of range and azimuth bins influence the accuracy of k calibration, Table II shows a comparison of the results obtained by the two algorithms with setting different numbers of range and azimuth bins. The amplitude and phase errors of k are

$$\begin{aligned} \text{error}_{\text{amp\_dB}} &= \text{mean}\left(\text{dB}\left|\frac{\text{Cal}\left(\text{amp}_k\right)}{\text{True}\left(\text{amp}_k\right)}\right|\right) \\ \text{error}_{\text{pha}} &= \text{mean}\left(\left|\text{Cal}\left(\text{pha}_k\right)-\text{True}\left(\text{pha}_k\right)\right|\right) \end{aligned} \tag{16}$$

where, $\text{error}_{\text{amp\_dB}}$ is the amplitude error in dB and $\text{error}_{\text{pha}}$ is the phase error in degrees. An examination of the data presented in Table II that calibration based on Halpha-UZH has better accuracy than Shi-UZH in most cases for different algorithms with the same azimuth and range blocks, except that shown in bold in Table II. At the same time, since the extraction accuracy of Shi-UZH mainly depends on fixed thresholds of ENL and R_{hhvv}, the preliminary results obtained by the calibration algorithm may deviate significantly from the real value, resulting in a large deviation after fitting, which is printed in italics in Table II. By contrast, this is not the case for Halpha-UZH.

When using the same algorithm with different azimuth and range directions, there is no evident regular trend along the azimuth direction or the range direction. By calculating the mean and variance of the errors in different distance directions respectively (Table II, rows 9–10), it is demonstrated that the calibration of k based on Halpha-UZH is more accurate and more stable than that using Shi-UZH.

Since the proposed method should be suitable for polarimetric applications in different scenarios where CRs cannot be deployed but requires accurate calibration of k, next, we use 24 multiscene simulated data by ALOS and GF-3 PolSAR images without CRs to further obtain more simulated results, that are presented in Fig. 6. Before carrying out the next step, the ALOS images are sampled every three pixels in the azimuth direction to ensure nearly equal values between the range and azimuth spacing, and the GF-3 images are sampled every five pixels in the azimuth and range directions to reduce data size.

The numbers of ext. BLPs under different data obtained by Halpha-UZH and Shi-UZH are shown in Fig. 6(a). Halpha-UZH is dominant in the quantity of selected points in nearly half of the data. The plots in Fig. 6(b) and (c) validate the number and the percentage of real BLPs in the ext. BLPs for all 24 simulated data points. With regard to the number of accurate points selected shown in Fig. 6(b), Halpha-UZH is superior to Shi-UZH for 17 of the 24 data points. It is observed from Fig. 6(c) that the accuracy of the points selected by Halpha-UZH is much higher compared to the accuracy of the points selected by Shi-UZH, showing that

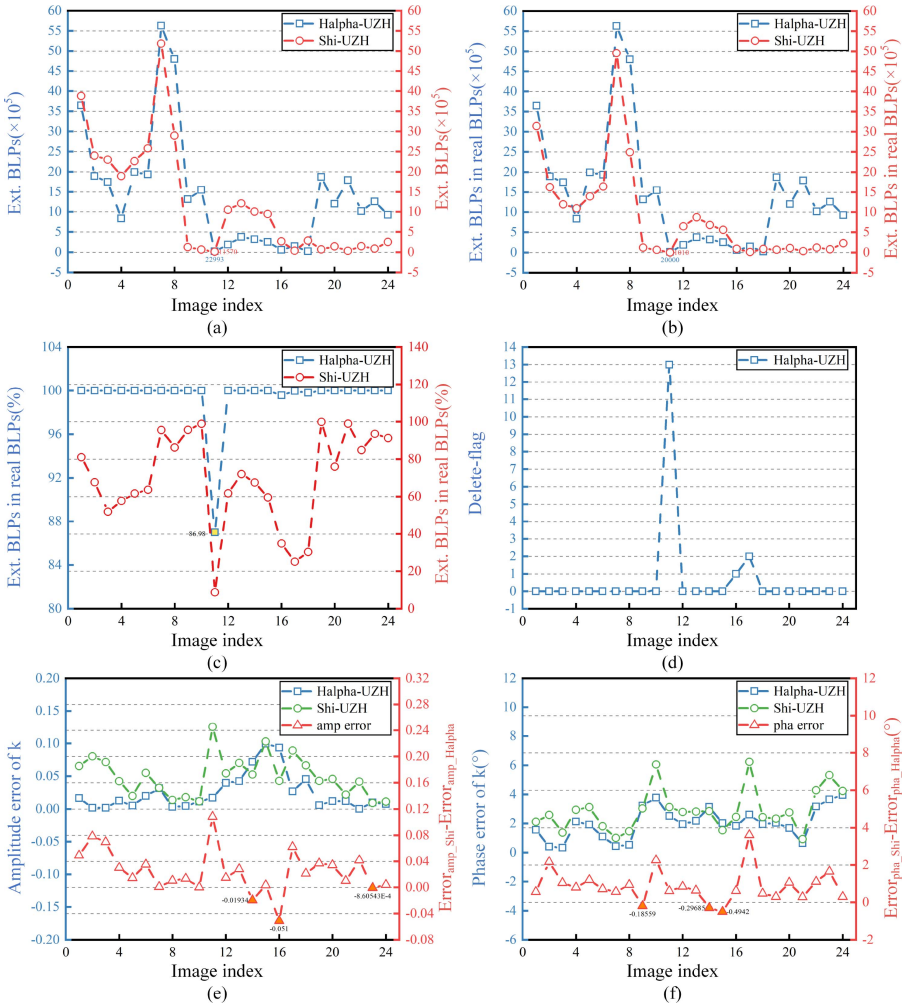

Fig. 6. 24 Simulated PolSAR data results obtained by Halpha-UZH and Shi-UZH. (a) Number of ext. BLPs (b) and (c) number and percentage of ext. BLPs in the Real BLPs. (d) Number of range cells that do not participate in fitting. (e) and (f) Amplitude and phase errors of k obtained by Halpha-UZH and Shi-UZH.

Halpha-UZH has a certain superiority over Shi-UZH with regard to the number and percentage of accurate extracted points.

Furthermore, only the No. 11 simulated PolSAR data do not reach more than 99% in the accuracy of the selected points. The No. 11 image mainly describes the urban area of Beijing, China, where trees, houses, and farmland are the main components. In Fig. 6(c), not all Z7 and Z8 points are fully distinguished from the NZ9 points, accounting for 13.02% of all selected points in No. 11 of the PolSAR images with k. This is most like because with the gradual reduction in φ_k, it is difficult to move the points closer to the boundary of NZ9. In addition, the number of ext. BLPs and the number of real BLPs in the ext. BLPs of No. 11. of the PolSAR images are shown in Fig. 6(a) and (b), which suggests that Halpha-UZH is much better than Shi-UZH in a complex multitype scattering environment with regard to the accuracy of the selected points.

In Step 4 of Section III-B, if the threshold of index_2 is not met within a certain range, the range data are removed to reduce the fitting error after UZH is used to obtain the preliminary results. Since the No. 11 data are mainly urban areas and contains fewer Bragg-like points, the sum of delete-flags is higher than for other simulated PolSAR data. Fig. 6(e) and (f) shows the amplitude error, phase error, and the relative error of the two methods after extracting BLPs through Halpha-UZH and Shi-UZH, and using UZH to perform the calibration process. To make the amplitude error more obvious, this parameter is expressed by (17) on the basis of (16)

$$\text{error}_{\text{amp}} = |10^{\text{error}_{\text{amp\_dB}}/20} - 1|. \tag{17}$$

Among the 24 selected data, the amplitude and phase results of 19 groups obtained by Halpha-UZH are comprehensively better than those obtained by Shi-UZH, showing that the calibration results of k can be improved by the quality and quantity of the selected points, with a particularly strong effect for the quality. However, not all experimental results obtained using Halpha-UZH are better than those of Shi-UZH, which are represented by orange triangles in Fig. 6(e) and (f). This is because the accuracy of the selected points is not the only factor that determines the calibration results; rather, the distribution of selected points in each range cell that affect the fitting process in [24] is also important. To summarize, based on the simulation data, the algorithm proposed in this article greatly improves the accuracy of extracting BLPs without CRs, and further strongly improves the calibration accuracy.

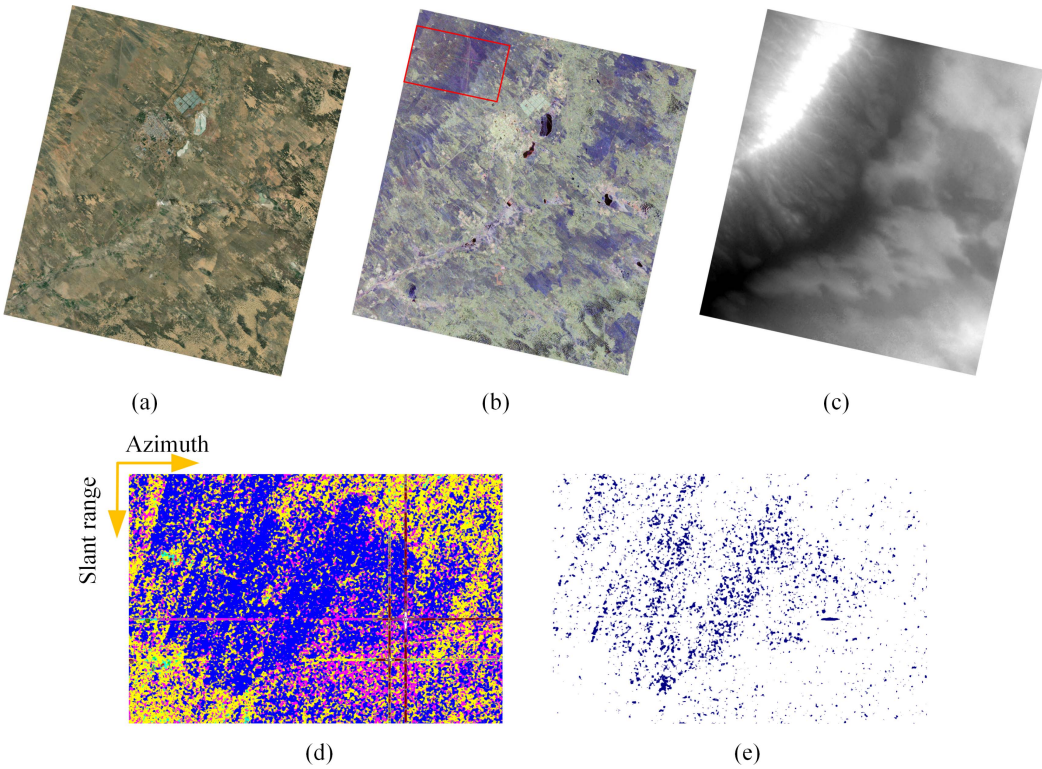

Fig. 7. GF-3 CR data. (a) Optical image of selected GF-3 data. (b) Pauli image of select GF-3 data. (c) Corresponding DEM of the selected GF-3 data by SRTM data. (d) Selected part $H/\bar{\alpha}$ decomposition of the GF-3 data by the red square in slant range direction. (e) Calculated UZH points of the selected GF-3 data.

B. CR Dataset

Since the PolSAR products used in the simulation dataset have residual calibration errors, the calibration results obtained based on the simulation data do not provide the real calibration accuracy of the image, but rather the calibration accuracy relative to the residual calibration error of the image. In this section, we use the reconstructed trihedral CRs to compare to those obtained directly in the image, and obtain the error of the reconstructed trihedral CRs, which can be considered as the calibration error of the image. The PolSAR data with CRs were acquired by the GF-3 calibration team in Inner Mongolia on September 19, 2019 [26]. To verify the calibration performance of the GF-3 system, China set up active radar calibrators, trihedral CRs, 0° dihedral CRs, and 45° rotated dihedral CRs. The optical and Pauli images of the CRs data are shown in Fig. 7(a) and (b), where the position of the CR is marked by the red box. Fig. 7(d) is the $H/\bar{\alpha}$ decomposition result corresponding to the red box in Fig. 7(b). To remove the influence of coherent speckle noise, the 7×7 multilook operator is used to estimate the coherency and covariance matrix in the subsequent image processing. Following ZeroAinsworth (Zero-Ans) calibration [13], [26] for XT and x-pol CI, Fig. 7(e) shows the BLPs of the Fig. 7(d) extracted by Halpha-UZH.

Since the resolution of the GF-3 image is 8 m and the edge length of five trihedral CRs is 1.235 m, the CR of each polarimetric channel is oversampled 16 times at the signal peak to analyse the preferments of CRs by the maximum method. As a trihedral CR, $|\mathrm{VV}/\mathrm{HH}|$ is usually defined to observe the unbalanced performance of the co-pol CI, and $|\mathrm{HV}/\mathrm{HH}|$ and $|\mathrm{VH}/\mathrm{HH}|$ to observe the XT. Table III shows the corresponding performance analysis of the five trihedral CRs in Fig. 7. Since the calibration model used is shown in (1), if the HV channel and the VH channel of a trihedral CR are observed at the same time, the reconstructed model based on calibration model should be changed according to

$$[O_{\mathrm{tri}}] = [X]\,[Q]\,[K_4]\,[S_{\mathrm{tri}}] = \begin{bmatrix} \chi & w & \chi v & wv \\ \chi u & 1 & \chi uv & v \\ \chi z & wz & \chi & w \\ \chi uz & z & \chi u & 1 \end{bmatrix} \begin{bmatrix} k^2 & 0 & 0 & 0 \\ 0 & k & 0 & 0 \\ 0 & 0 & k & 0 \\ 0 & 0 & 0 & 1 \end{bmatrix} \begin{bmatrix} 1 \\ 0 \\ 0 \\ 1 \end{bmatrix} \tag{18}$$

where, $[O_{\mathrm{tri}}]$ and $[S_{\mathrm{tri}}]$ are, respectively, the vector format of the observation scattering matrix and nondistorted scattering matrix of a trihedral CR.

Tables IV, V, and VI provide the XT and CI of different $[O_{\mathrm{tri}}]$ obtained by using the Ans, Zero-Ans, and Quegan algorithms [12], [13] to determine XT and x-pol CI, and UZH to determine the co-pol CI, respectively. In addition, The BLPs for UZH are provided by Halpha-UZH and Shi-UZH. It is clearly observed that 1) under the same algorithm for extracting BLPs, the accuracy is significantly higher for the Zero-Ans algorithm and the Ans algorithm in $|\mathrm{VV}/\mathrm{HH}|$ compared to that of the Quegan algorithm, and $|\mathrm{HV}/\mathrm{HH}|$ and $|\mathrm{VH}/\mathrm{HH}|$ is underestimated in most cases. In particular, the underestimation is more pronounced for the Ans algorithm is more prominent than for the other algorithms. 2) With the same algorithm used to calibrate XT and x-pol CI, solving

TABLE III
QUALITY EVALUATION OF FIVE TRIHEDRAL CRS IN THE GF-3 DATA. THE UNIT OF MEASURE IN THE SECOND ROW, THE FOURTH ROW AND THE FIFTH ROW IS DB, AND THE UNIT OF MEASURE IN THE THIRD ROW IS DEGREES (°)

	Tr.1	Tr.2	Tr.3	Tr.4	Tr.5
$\lvert VV/HH\rvert$	0.4483	0.337	0.402	0.2031	0.3415
$\angle VV/HH$	4.9495	5.1914	7.4692	4.1844	4.163
$\lvert HV/HH\rvert$	−36.432	−36.9176	−35.2844	−37.7011	−39.1406
$\lvert VH/HH\rvert$	−35.9448	−36.4782	−36.7487	−38.3515	−39.794

TABLE IV
u, v, w, z, AND χ RESULTS OBTAINED BY THE ZERO-ANS ALGORITHM

		Tr.1	Tr.2	Tr.3	Tr.4	Tr.5
Halpha-UZH	$\lvert VV/HH\rvert$	0.2836	0.3963	0.4286	0.4367	0.4448
	$\angle VV/HH$	3.162	6.3403	7.2483	7.4753	7.7024
	$\lvert HV/HH\rvert$	−38.2544	−37.9338	−37.8444	−37.8222	−37.8000
	$\lvert VH/HH\rvert$	−45.0475	−44.7898	−44.7163	−44.698	−44.6796
Shi-UZH	$\lvert VV/HH\rvert$	−0.2929	−0.2888	−0.2877	−0.2874	−0.2871
	$\angle VV/HH$	0.6391	0.1592	0.0221	−0.0122	−0.0465
	$\lvert HV/HH\rvert$	−38.682	−38.725	−38.7373	−38.7404	−38.7435
	$\lvert VH/HH\rvert$	−45.229	−45.2666	−45.2773	−45.28	−45.2827

TABLE V
u, v, w, z, AND χ RESULTS OBTAINED BY THE ANS ALGORITHM

		Tr.1	Tr.2	Tr.3	Tr.4	Tr.5
Halpha-UZH	$\lvert VV/HH\rvert$	0.3030	0.3448	0.3565	0.3590	0.3624
	$\angle VV/HH$	−2.2677	−0.1619	0.4398	0.5902	0.7406
	$\lvert HV/HH\rvert$	−45.9583	−45.8599	−45.8326	−45.8258	−45.8191
	$\lvert VH/HH\rvert$	−46.4726	−46.3741	−46.3469	−46.3401	−46.3334
Shi-UZH	$\lvert VV/HH\rvert$	0.2348	0.1541	0.1310	0.1250	0.1190
	$\angle VV/HH$	−1.4454	−2.3317	−2.5849	−2.6482	−2.7115
	$\lvert HV/HH\rvert$	−45.8795	−45.9186	−45.9300	−45.9328	−45.9357
	$\lvert VH/HH\rvert$	−46.3937	−46.4329	−46.4442	−46.4471	−46.4499

TABLE VI
u, v, w, z, AND χ RESULTS OBTAINED BY THE QUEGAN ALGORITHM

		Tr.1	Tr.2	Tr.3	Tr.4	Tr.5
Halpha-UZH	$\lvert VV/HH\rvert$	−0.6156	−0.4036	−0.3425	−0.3272	−0.3119
	$\angle VV/HH$	5.5927	8.7977	9.7134	9.9423	10.1712
	$\lvert HV/HH\rvert$	−37.5782	−37.1956	−37.0872	−37.0602	−37.0332
	$\lvert VH/HH\rvert$	−44.2809	−44.0552	−43.9862	−43.9686	−43.9510
Shi-UZH	$\lvert VV/HH\rvert$	−0.9291	−0.7491	−0.6974	−0.6844	−0.6714
	$\angle VV/HH$	1.9830	0.1654	−0.3540	−0.4838	−0.6136
	$\lvert HV/HH\rvert$	−38.0280	−38.2017	−38.2530	−38.2660	−38.2789
	$\lvert VH/HH\rvert$	−44.4693	−44.7020	−44.7706	−44.7879	−44.8052

$|VV/HH|$ by Halpha-UZH is more advantageous than solving by Shi-UZH. The reconstructed errors shown in Table VII also confirm the higher precision of the k calibration based on Halpha-UZH.

V. DISCUSSION

Because Halpha-UZH incorporates some arbitrary factors, such as threshold selection, that affect the accuracy of Halpha-UZH, a detailed discussion of these problems is presented in this section.

A. R_{xc}: Threshold Selection of cod_1 and cod_2

In the proposed algorithm, cod_1 and cod_2 are utilized to select the preliminary BLPs. In calibrating k, different feature types and distribution characteristics directly affect how to select R_{xc}. In Fig. 8, we use two new parameters to show the impact of R_{xc} in experimental scenes Nos. 1–24, which can be written as

$$\mathrm{cod}_3 = 10 * \log_{10}\left(\frac{|C_{22}|^2}{|C_{11}|}\right)$$

TABLE VII
MEAN AMPLITUDE ERROR (DB) AND PHASE ERROR (°) EVALUATION BY CRS ON |VV/HH|

		Zero-Ans	Ans	Quegan
Halpha-UZH	Amplitude	0.1175	0.0751	0.7465
	Phase	1.9975	5.3233	3.6520
Shi-UZH	Amplitude	0.6352	0.1936	1.0927
	Phase	5.0392	7.5358	5.0521

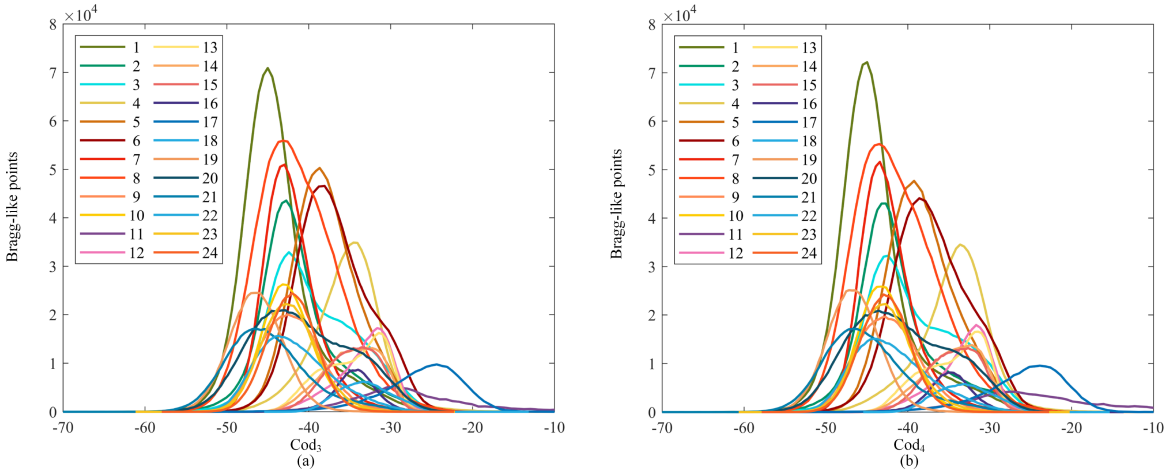

Fig. 8. Quantity of BLPs in different (a) cod_3 and (b) cod_4 situations by different PolSAR data. The legends represent the identifiers of PolSAR image data corresponding to Fig. 3.

$$\text{cod}_4 = 10 * \log_{10}\left(\frac{|C_{22}|^2}{|C_{33}|}\right). \tag{19}$$

The relationship between (19) and (14) is given by

$$\text{cod}_1 = 10 * \log_{10}\left(\frac{|O_{22}|^2}{|O_{11}|}\right) = 10 * \log_{10}\left(\frac{|C_{22}|^2}{|C_{11}|}\right)$$

$$\text{cod}_2 = 10 * \log_{10}\left(\frac{|O_{22}|^2}{|O_{33}|}\right)$$

$$= 20 * \log_{10}(|k|) + 10 * \log_{10}\left(\frac{|C_{22}|^2}{|C_{33}|}\right). \tag{20}$$

It is clear that cod_1 is equal to cod_3 and that the value range of cod_2 is $-2 + \text{cod}_4 \sim 2 + \text{cod}_4$ because the amplitude of k is -2 to 2 dB. Fig. 8(a) and (b) shows the number of BLPs in different cod_3 and cod_4 situations. It is observed that cod_3 and cod_4 of almost all BLPs are less than -20 dB. Similarly, cod_1 and cod_2 are the same, although the maximum of cod_2 is cod_4+2, except for PolSAR images Nos. 11 and 17 that contain volume and double-bounce scattering targets. Considering that the dynamic extraction is proposed to select most of the BLPs in the uncalibrated k PolSAR data first and then select the accurate BLPs through the phase shift of k, it is appropriate to set R_{xc} at -20 dB after checking all experimental data. Note that although non-BLPs may be selected by the R_{xc} threshold, the displacement of the $H/\bar{\alpha}$ plane by subsequently adding the φ_k is more orderly, which means that the whole plane tends to reflect the characteristics of real features rather than being more disorderly. In other words, the threshold set by R_{xc} provides only a reference rather than a decision for the last selected points.

B. Threshold Selection of index_2

When we select the BLPs by taking into account the influences of the selected points in each bin and the BLPs in the selected points of NZ9, we obtain the maximum value of index_1 by adding each φ_k. The index_2 greater than 0.9 at this maximum value is considered to ensure better calibration results due to the more accurate selection of BLPs. When the stopping condition is reached, the range cell whose index_2 is less than 0.9 does not participate in the next calibration operation to reduce the calibration error of k. If the threshold of index_2 is set to a lower value, then the value of index_1 may be dominated by the number of ext. BLPs, and there may exist more non-BLPs that are on the boundary of NZ9 and Z8 in the $H/\bar{\alpha}$ plane, resulting in low fitting accuracy for calibrating k. However, it can be clearly seen that after extracting BLPs by the threshold of index_2, the real BLPs still move to NZ9 by adding $[K_{\text{pha3}}]$ to the uncalibrated k PolSAR images, as can be seen by the maximum number change of the ext. BLPs under different thresholds of index_2.

Fig. 9 shows different fitting error results obtained by the antithetic threshold of index_2 in Nos. 1–24 of the experimental datasets, namely 0.70, 0.80, 0.90, 0.91, 0.92, 0.93, 0.94, and 0.95. The number of range bins is 80, and the azimuth size of a bin is 80. R_{xc} is set at -20 dB. Fig. 9(a) and (b) represents the ext. BLPs and the number of real BLPs in the ext. BLPs in

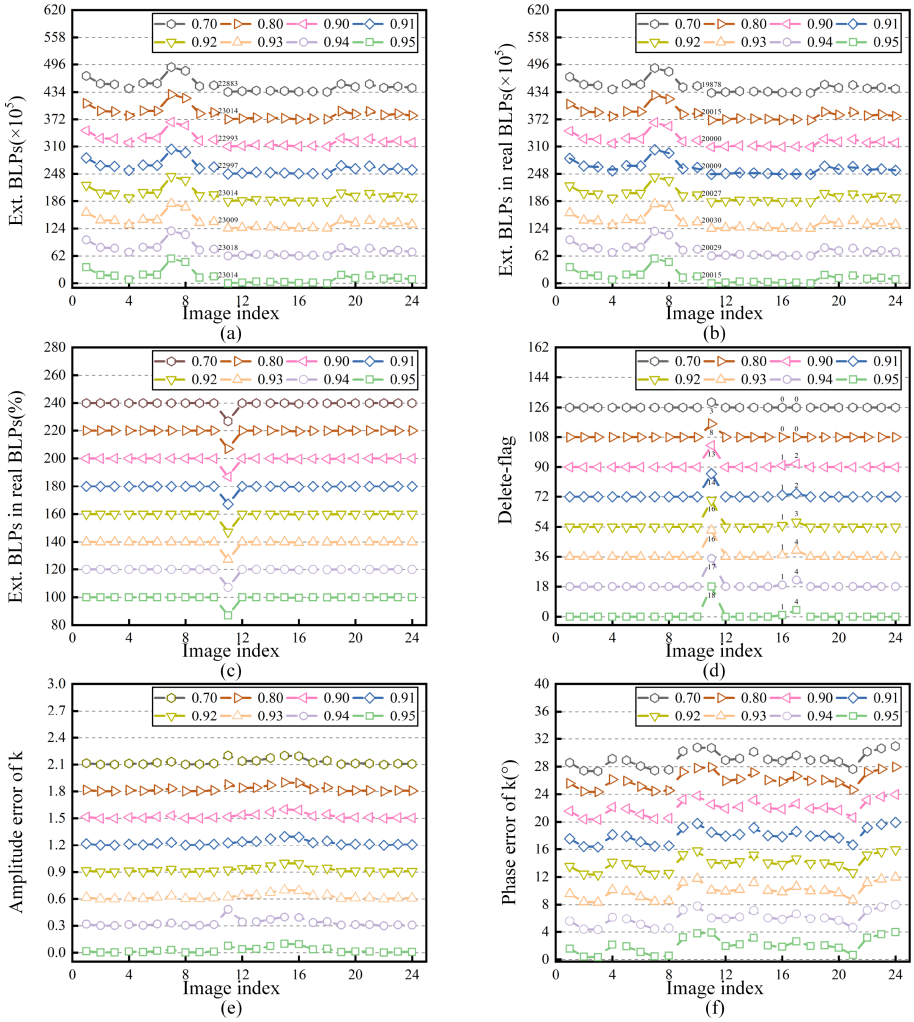

Fig. 9. *Y*-axis offset diagram of different PolSAR data results obtained by eight index$_2$ thresholds, namely 0.95, 0.94, 0.93, 0.92, 0.91, 0.9, 0.8, and 0.7. The offsets of (a)–(f) are 62×10^5, 62×10^5, 20%, 18, 0.3, and 4°. (a) Number of ext. BLPs. (b) and (c) Number and percentage of ext. BLPs in the real BLPs. (d) Number of range cells that do not participate in fitting. (e) and (f) Amplitude and phase errors of k obtained by Halpha-UZH and Shi-UZH.

the selected points according to Halpha-UZH. Fig. 9(c) shows the percentage of the real BLPs in the ext. BLPs. When the threshold of index$_2$ is set to the abovementioned numbers, it does not affect the number of final ext. BLPs and the number of real BLPs in most cases. In a few cases, it is possible that after adding $[K_{\text{pha3}}]$ to the uncalibrated k PolSAR images, more points in Z7 and Z8 move to or away from NZ9 since the two weights of index_1 are similar. Furthermore, even if affected, the subsequent smaller angle cycle does not have a strong impact on the selected points, and the difference in the number of points in this case is less than 200 according to the results of the experiments presented in Fig. 9(a) and (b).

In Fig. 9(a) and (b), the maximum difference between any two numbers is 135 and 152, respectively, under the same abscissa. Fig. 9(d) indicates how many range cells in the experimental data do not participate in the fitting operation because the threshold of index$_2$ is not reached. In Fig. 9(e) and (f), the amplitude errors and phase errors of k remain unchanged in most cases due to the invariance of the selected points and the correct points or the small number of range cells in the No. 16 experimental image that do not participate in fitting. However, in some rare cases, the amplitude errors and phase errors indeed change. According to Fig. 9, the most important reason affecting the error changes of Nos. 11 and 16 is the number of delete flags. Considering the accuracy of the selected points and the number of delete flags, we recommend setting the index x_2 threshold at 0.9 to obtain a higher accuracy of the selected points and to maximize the number of range cells used for fitting.

C. $\pm45°$: *Initial Degrees of* φ_k

According to the derivation in (12), an interesting regulation suggests that points on the $H/\bar{\alpha}$ plane exhibit an oscillating change of a trigonometric function with the period of 180° by changing φ_k. In Section III-B, this derivation is implemented when extracting the BLPs. Simultaneously, when the points on the $H/\bar{\alpha}$ plane are moved by adding φ_k, we utilize $\pm45°$ as the initial value. In the following, we explain why this parameter is set to 45°.

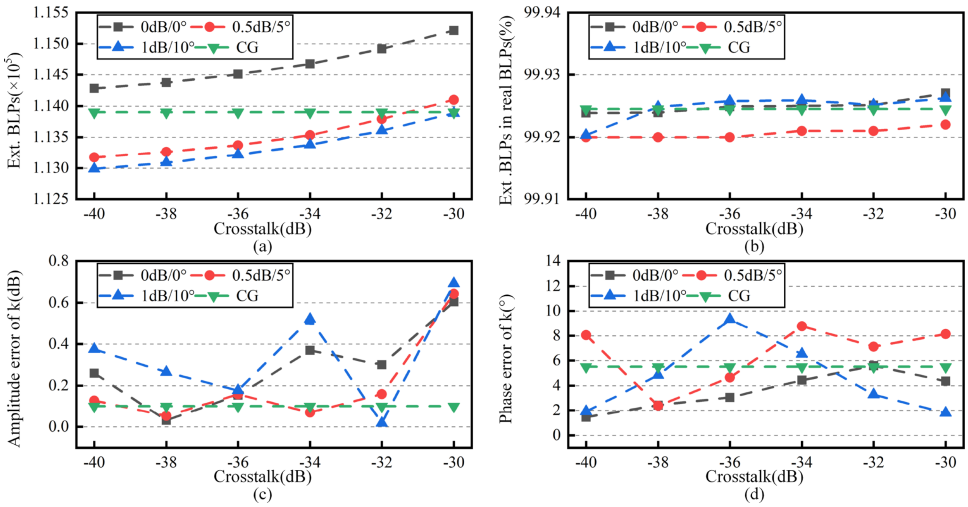

Fig. 10. Whole calibration process errors when XT (from −40 to −30 dB) and x-pol CI (0 dB/0°, 0.5 dB/5°, and 1 dB/10°) are imposed. The green lines (CG) represent the condition without XT and x-pol CI. (a) Number of calculated BLPs. (b) Percentage of ext. BLPs in the real BLPs. (c)–(d) Amplitude and phase errors of k.

Considering that the periodic change is 180°, it can be determined that the change interval of the independent variable becomes −90° to 90°. Then, we artificially divide −90° to 90° into two parts, that is, −90° to 0° and 0° to 90°. At each interval, the most representative angle is the intermediate angle. Therefore, it is acceptable to solve the problem by setting the initial value in the middle of the two intervals. Therefore, we set the initial degrees of φ_k as $\pm 45°$. This can also explain why we choose $\pm 45/2^i$ as the angle of adding k for our subsequent angle moves during the ith loop.

D. Error of Calibrating k Caused by Residual XT and X-Pol CI

Since the algorithm proposed in this article extracts the BLPs for calibrating k, all formulas and solution algorithms in this article are based on the absence of XT and x-pol CI in PolSAR systems. Residual XT and x-pol CI are inevitable and should be considered when extracting BLPs. By analyzing the nominal PolCAL accuracies of PolSAR sensors [15], [23], [40], [41], the residual XT and residual CIs are better than −30 dB and ± 0.5 dB/10°, respectively. Next, XT with −40 to 30 dB and x-pol CI with 0 dB/0°, 0.5 dB/5°, and 1 dB/10° are added to the AIRSAR simulation data to analyze the impact on the ext. BLPs and calibration of k. The numbers of range bins and azimuth bins are 80 and 60, respectively.

The results are shown in Fig. 10, where the green lines indicate the results without any XT and x-pol CI. In Fig. 10(a), as the residual XT increases, an increasing number of BLPs are selected. However, the opposite is true for the residual x-pol CI. Considering that the percentage of ext. BLPs in the real BLPs shown in Fig. 10(b) is almost unchanged, it can be conducted from the comparison with the green lines that XT can increase the number of ext. BLPs in the real BLPs, while the opposite is the case for the x-pol CI. Fig. 10(c) and (d) shows the amplitude error and phase error of k, respectively. XT is the main influencing factor of the amplitude error. However, the the effects of the residual XT and x-pol CI on the phase error are unpredictable. Considering the green lines in these two figures, it may be possible to reduce the influence of residual XT and x-pol CI by increasing the quality and quantity of selected points, particularly with regard to the amplitude error. Therefore, there is a vast space to reconsider the exact impact of XT and x-pol CI on the calibration model of UZH and modify them to enhance the accuracy of k.

VI. Conclusion

In this article, we propose a BLP extraction method by using H and $\bar{\alpha}$ from uncalibrated k PolSAR images. We perform simulated and actual data analysis on AIRSAR, ALOS, and GF-3 data. For the experimental results, the real BLPs account for more than 99% of all ext. BLPs in the majority data. The k calibration by the ext. BLPs extracted by Halpha-UZH is better than that for Shi-UZH and is very close to the measurement of trihedral CRs. After using the Ans, Zero-Ans, and Quegan algorithms to perform calibration of XT and x-pol CI, the smallest average error amplitude is 0.0751 dB, and the smallest phase is 1.9975° in calibrating k obtained by Halpha-UZH.

The main idea in this article of selecting BLPs is to use H and $\bar{\alpha}$ to find some of the Z9 points with the property of zero helicity from uncalibrated k PolSAR images. In Section V, it is found that the residual XT and x-pol CI have different effects on the scatter characteristics of targets on the $H/\bar{\alpha}$ plane, which is an interesting topic for further analysis. In the framework proposed in this article, since the points of Z9 are mainly affected by the Z6 points when we change only the amplitude of k in the $H/\bar{\alpha}$ plane, the ext. BLPs are calculated from NZ9 rather than Z9. Therefore, some of the Z9 points are discarded after setting the limit. If the discarded points can also be fully utilized, it is quite likely that the accuracy of selecting BLPs will be improved, and we plan to examine this topic in the future.

APPENDIX

When the amplitude of k is constant and the phase is changed, we hypothesize that the eigenvalue of $[O]$ is unaffected. This appendix presents the corresponding mathematical derivation process. Since we consider the amplitude and phase of k separately, (10) can be rewritten as

$$[O] = [K_{\text{pha3}}]\,[K_{\text{amp3}}]\,[C_3]\,[K_{\text{amp3}}]^H\,[K_{\text{pha3}}]^H \tag{21}$$

$$[K_{\text{amp3}}] = \begin{bmatrix} |k|^2 & 0 & 0 \\ 0 & |k| & 0 \\ 0 & 0 & 1 \end{bmatrix} \tag{22}$$

$$[K_{\text{pha3}}] = \begin{bmatrix} e^{2j*\varphi_k} & 0 & 0 \\ 0 & e^{j\varphi_k} & 0 \\ 0 & 0 & 1 \end{bmatrix} \tag{23}$$

where, $|\cdot|$ represents the absolute value operation and φ_k is the phase of k. According to the definition of the covariance matrix, it can be obtained that $[C_3]$ is a Hermitian matrix. Since we consider only the change in φ_k and $|k|$ is unchanged, we define $[C_3']$ as

$$[C_3'] = [K_{\text{amp3}}]\,[C_3]\,[K_{\text{amp3}}]^H. \tag{24}$$

Since $[K_{\text{amp3}}]$ is a diagonal matrix, $[C_3']$ is a Hermitian matrix. Considering that $[K_{\text{pha3}}]$ is a unitary matrix and the unitary transformation of a Hermitian matrix does not change the eigenvalues, the eigenvalues of $[O]$ and $[C_3']$ are the same. That is, when $[C_3]$ is affected by k, the eigenvalue of $[O]$ is unchanged if the amplitude of k is constant and the phase is changed.

ACKNOWLEDGMENT

The authors would like to thank the Alaska Satellite Facility for providing the AIRSAR and ALOS data. They also thank Wentao Hou for helpful discussions.

REFERENCES

[1] M. Arii, H. Yamada, H. Sakamoto, and S. Kojima, "Sensitivity study of X-band multiparametric SAR data from cabbage fields," *IEEE Trans. Geosci. Remote Sens.*, vol. 60, 2022, Art. no. 5203611.

[2] F. Shang, T. Saito, S. Ohi, and N. Kishi, "Coniferous and broad-leaved forest distinguishing using L-band polarimetric SAR data," *IEEE Trans. Geosci. Remote Sens.*, vol. 59, no. 9, pp. 7487–7499, Sep. 2021.

[3] N. Longepe, A. A. Mouche, L. Ferro-Famil, and R. Husson, "Co-cross-polarization coherence over the sea surface from Sentinel-1 SAR data: Perspectives for mission calibration and wind field retrieval," *IEEE Trans. Geosci. Remote Sens.*, vol. 60, 2022, Art. no. 4200816.

[4] A. Patil, G. Singh, C. Rudiger, S. Mohanty, and Snehmani, "A novel approach for the snow water equivalent retrieval using X-band polarimetric synthetic aperture radar data," *IEEE Trans. Geosci. Remote Sens.*, vol. 59, no. 5, pp. 3753–3763, May 2021.

[5] A. Freeman, "SAR calibration: An overview," *IEEE Trans. Geosci. Remote Sens.*, vol. 30, no. 6, pp. 1107–1121, Nov. 1992.

[6] A. Freeman, Y. Shen, and C. L. Werner, "Polarimetric SAR calibration experiment using active radar calibrators," *IEEE Trans. Geosci. Remote Sens.*, vol. 28, no. 2, pp. 224–240, Mar. 1990.

[7] J. J. V. Zyl, "Calibration of polarimetric radar images using only image parameters and trihedral corner reflector responses," *IEEE Trans. Geosci. Remote Sens.*, vol. 28, no. 3, pp. 337–348, May 1990.

[8] W. M. Whitt, F. T. Ulaby, P. Polatin, and V. V. Liepa, "A general polarimetric radar calibration technique," *IEEE Trans. Antennas Propag.*, vol. 39, no. 1, pp. 62–67, Jan. 1991.

[9] L. Zhu et al., "The polarimetric l-band imaging synthetic aperture radar (PLIS): Description, calibration, and cross-validation," *IEEE J. Sel. Topics Appl. Earth Observ. Remote Sens.*, vol. 11, no. 11, pp. 4513–4525, Nov. 2018.

[10] J. Lin, Y. Guo, W. Li, Y. Zhang, and Z. Chen, "Polarimetric calibration based on lexicographic-basis decomposition," *IEEE Geosci. Remote Sens. Lett.*, vol. 13, no. 8, pp. 1149–1152, Aug. 2016.

[11] L. Li, Y. Zhu, J. Hong, F. Ming, and Y. Wang, "Design and implementation of a novel polarimetric active radar calibrator for Gaofen-3 SAR," *Sensors*, vol. 18, no. 8, 2018, Art. no. 2620.

[12] S. Quegan, "A unified algorithm for phase and cross-talk calibration of polarimetric data-theory and observations," *IEEE Trans. Geosci. Remote Sens.*, vol. 32, no. 1, pp. 89–99, Jan. 1994.

[13] T. L. Ainsworth, L. Ferro-Famil, and J. S. Lee, "Orientation angle preserving a posteriori polarimetric SAR calibration," *IEEE Trans. Geosci. Remote Sens.*, vol. 44, no. 4, pp. 994–1003, Apr. 2006.

[14] A. Villa, L. Iannini, D. Giudici, A. Monti-Guarnieri, and S. Tebaldini, "Calibration of SAR polarimetric images by means of a covariance matching approach," *IEEE Trans. Geosci. Remote Sens.*, vol. 53, no. 2, pp. 674–686, Feb. 2015.

[15] Y. Chang, P. Li, J. Yang, J. Zhao, L. Zhao, and L. Shi, "Polarimetric calibration and quality assessment of the GF-3 satellite images," *Sensors*, vol. 18, no. 2, p. 403, 2018.

[16] Y. Changet al., "Polarimetric calibration of SAR images using reflection symmetric targets with low helix scattering," *Int. J. Appl. Earth Observ. Geoinformation*, vol. 104, 2021, Art. no. 102559.

[17] G. Sun, Z. Li, L. Huang, Q. Chen, and P. Zhang, "Quality analysis and improvement of polarimetric synthetic aperture radar (SAR) images from the Gaofen-3 satellite using the amazon rainforest as an example," *Int. J. Remote Sens.*, vol. 42, no. 6, pp. 2131–2154, 2021.

[18] A. Maiti, S. Kumar, V. Tolpekin, and S. Agarwal, "A computationally efficient hybrid framework for polarimetric calibration of quad-pol SAR data," *Earth Space Sci.*, vol. 8, no. 3, 2021, Art. no. e2020EA001447.

[19] S. R. Cloude, "Calibration of polarimetric radar data using the Sylvester equation in a Pauli basis," 2021, *arXiv:2111.04565*.

[20] M. Shimada, "Model-based polarimetric SAR calibration method using forest and surface-scattering targets.," *IEEE Trans. Geosci. Remote Sens.*, vol. 49, no. 5, pp. 1712–1733, May 2011.

[21] L. Shi, J. Yang, and P. Li, "Co-polarization channel imbalance determination by the use of bare soil," *ISPRS J. Photogrammetry Remote Sens.*, vol. 95, no. 9, pp. 53–67, 2014.

[22] L. Shi, P. Li, J. Yang, L. Zhang, X. Ding, and L. Zhao, "Co-polarization channel imbalance phase estimation by corner-reflector-like targets," *ISPRS J. Photogrammetry Remote Sens.*, vol. 147, pp. 255–266, 2019.

[23] S. Jiang, X. Qiu, B. Han, and W. Hu, "A quality assessment method based on common distributed targets for GF-3 polarimetric SAR data," *Sensors*, vol. 18, no. 3, p. 807, 2018.

[24] L. Shi, P. Li, J. Yang, L. Zhang, X. Ding, and L. Zhao, "Polarimetric SAR calibration and residual error estimation when corner reflectors are unavailable," *IEEE Trans. Geosci. Remote Sens.*, vol. 58, no. 6, pp. 4454–4471, Jun. 2020.

[25] S. Shangguan, X. Qiu, K. Fu, B. Lei, and W. Hong, "GF-3 polarimetric data quality assessment based on automatic extraction of distributed targets," *IEEE J. Sel. Topics Appl. Earth Observ. Remote Sens.*, vol. 13, pp. 4282–4294, 2020.

[26] L. Shi, P. Li, J. Yang, H. Sun, L. Zhao, and L. Zhang, "Polarimetric calibration for the distributed Gaofen-3 product by an improved unitary zero helix framework," *ISPRS J. Photogrammetry Remote Sens.*, vol. 160, pp. 229–243, 2020.

[27] S. R. Cloude and E. Pottier, "A review of target decomposition theorems in radar polarimetry," *IEEE Trans. Geosci. Remote Sens.*, vol. 34, no. 2, pp. 498–518, Mar. 1996.

[28] J. Praks and M. Hallikainen, "A novel approach in polarimetric covariance matrix eigendecomposition," in *Proc. IEEE Int. Geosci. Remote Sens. Symp. Taking Pulse Planet: Role Remote Sens. Manag. Environ. Proc.*, 2000, vol. 3 pp. 1119–1121.

[29] S. R. Cloude, R. Ossikovski, and E. Garcia-Caurel, "Bright singularities: Polarimetric calibration of spaceborne PolSAR systems," *IEEE Geosci. Remote Sens. Lett.*, vol. 18, no. 3, pp. 476–479, Mar. 2021.

[30] S. R. Cloude and E. Pottier, "An entropy based classification scheme for land applications of polarimetric SAR," *IEEE Trans. Geosci. Remote Sens.*, vol. 35, no. 1, pp. 68–78, Jan. 1997.

[31] C. Wang, W. Yu, R. Wang, Y. Deng, and F. Zhao, "Comparison of nonnegative eigenvalue decompositions with and without reflection symmetry assumptions," *IEEE Trans. Geosci. Remote Sens.*, vol. 52, no. 4, pp. 2278–2287, Apr. 2014.

[32] K. Sarabandiet al., "Polarimetric calibration of SIR-C using point and distributed targets," *IEEE Trans. Geosci. Remote Sens.*, vol. 33, no. 4, pp. 858–866, Jul. 1995.
[33] R. Touzi and M. Shimada, "Calibration and validation of polarimetric ALOS2," in *Proc. IEEE Int. Geosci. Remote Sens. Symp.*, 2015, pp. 4113–4116.
[34] A. Luscombe, "Image quality and calibration of RADARSAT-2," in *Proc. IEEE Int. Geosci. Remote Sens. Symp.*, 2009, vol. 2, pp. II-757–II-760.
[35] S. Jiang, X. Qiu, B. Han, J. Sun, and C. Ding, "Error source analysis and correction of GF-3 polarimetric data," *Remote Sens.*, vol. 10, no. 11, 2018, Art. no. 1685.
[36] J. Praks, E. C. Koeniguer, and M. T. Hallikainen, "Alternatives to target entropy and alpha angle in SAR polarimetry," *IEEE Trans. Geosci. Remote Sens.*, vol. 47, no. 7, pp. 2262–2274, Jul. 2009.
[37] F. T. Ulaby, T. F. Haddock, and R. T. Austin, "Fluctuation statistics of millimeter-wave scattering from distributed targets," *IEEE Trans. Geosci. Remote Sens.*, vol. 26, no. 3, pp. 268–281, May 1988.
[38] J.-S. Lee, M. R. Grunes, and R. Kwok, "Classification of multi-look polarimetric SAR imagery based on complex Wishart distribution," *Int. J. Remote Sens.*, vol. 15, no. 11, pp. 2299–2311, 1994.
[39] J. Lee, D. Schuler, R. Lang, and K. Ranson, "K-distribution for multi-look processed polarimetric SAR imagery," in *Proc. IEEE Int. Geosci. Remote Sens. Symp.*, 1994, pp. 2179–2181, vol. 4.
[40] T. Motohka, O. Isoguchi, M. Sakashita, and M. Shimada, "Results of ALOS-2 PALSAR-2 calibration and validation after 3 years of operation," in *Proc. IEEE Int. Geosci. Remote Sens. Symp.*, 2018, pp. 4169–4170.
[41] R. Caves, "RADARSAT-2 polarimetric calibration performance over five years of operation," in *Proc. 10th Eur. Conf. Synthetic Aperture Radar*, 2014, pp. 1–4.

Xingjie Zhao was born in Xingtai, China, in 1998. He received the B.S. degree in electronic and information engineering from Northwestern Polytechnical University, Xi'an, China, in 2019. He is currently working toward the Ph.D. degree with the Department of Space Microwave Remote Sensing System, Aerospace Information Research Institute, Chinese Academy of Sciences, Beijing, China.

He is currently with the University of Chinese Academy of Sciences, Beijing, China. His research interests include polarimetric synthetic aperture radar information extraction and calibration.

Yunkai Deng (Member, IEEE) received the M.S. degree in electrical engineering from the Beijing Institute of Technology, Beijing, China, in 1993.

He is currently a Research Scientist with the University of Chinese Academy of Sciences, Beijing, China. In 1993, he was with the Institute of Electronics, Chinese Academy of Sciences (IECAS), Beijing, where he was involved in antenna design, microwave circuit design, and spaceborne/airborne synthetic-aperture radar (SAR) technology. Since 1993, he has been a Research Fellow with the Department of Space Microwave Remote Sensing System, IECAS. He has been the Leader of several spaceborne/airborne SAR programs and developed some key technologies of spaceborne/airborne SAR. Since 2012, he has been a Principal Investigator with the Helmholtz-Chinese Academy of Sciences (CAS) Joint Research Group, Beijing, concerning Spaceborne Microwave Remote Sensing for Prevention and Forensic Analysis of Natural Hazards and Extreme Events. He has authored or coauthored more than 100 articles since 2002, of which more than 100 peer-reviewed and well-known journal articles. His research interests include spaceborne/airborne SAR technology for advanced modes, multifunctional radar imaging, and microwave circuit design.

Mr. Deng is a Member of the Scientific Board. He was a recipient of several prizes, including the First and Second Class Rewards of National Defense Science and Technology Progress in 2007, the First Class Reward of the National Scientific and Technological Progress in 2008, the achievements of the Outstanding Award of the CAS in 2009, and the First Class Reward of Army Science and Technology Innovation in 2016, for his outstanding contribution in SAR field.

Hanglan Guo received the B.S. degree in electronic and information engineering from the Harbin Institute of Technology, WeiHai, China, in 2019. She is currently working toward the Ph.D. degree with the Department of Space Microwave Remote Sensing System, Aerospace Information Research Institute, Chinese Academy of Sciences, Beijing, China.

She is currently with the University of Chinese Academy of Sciences, Beijing. Her research interests include polarimetric synthetic aperture radar calibration and validation.

Xiuqing Liu graduated from the Institute of Electronics, Chinese Academy of Sciences, Beijing, China, and received the Ph.D. degree in communication and information systems, in January 2004.

She is currently an Associate Researcher with Aerospace Information Research Institute, Chinese Academy of Sciences. She has hosted one National Natural Science Foundation project; participated as an important member of one National 863 Key Project and four National Major Projects. She has conducted systematic research on information extraction, such as SAR, polarimetric SAR image and data filtering, data compensation, image enhancement, clutter suppression, image classification, inversion, and polarization interference synthetic aperture radar data processing. She has authored or coauthored more than 20 papers and applied for 20 national invention patents. Her research interests include polarimetric SAR information processing and application. She is mainly engaged in research on SAR/ polarimetric SAR image processing and information extraction.

Chunle Wang received the B.S. degree from Beijing Information Science and Technology University, Beijing, China, in 2008, and the Ph.D. degree from the Graduate University of Chinese Academy of Sciences, Beijing, in 2013.

She is currently an Associate Research Assistant of SAR system design and their image processing with the Institute of Electronic, Chinese Academy of Science. Her research interests include classification and polarimetric target decomposition technique for polarimetric synthetic aperture radar with the University of Chinese Academy of Science.

Guo Song received the B.S. degree in aerospace engineering from Tsinghua University, Beijing, China, in 2019. He is currently working toward the Ph.D. degree with the Department of Space Microwave Remote Sensing System, Aerospace Information Research Institute, Chinese Academy of Sciences, Beijing.

He is currently with the University of Chinese Academy of Sciences, Beijing. His research interests include compact polarimetric synthetic aperture radar decomposition and classification.